

## ORIGAMI: DELINEATING HALOS USING PHASE-SPACE FOLDS

BRIDGET L. FALCK, MARK C. NEYRINCK, AND ALEXANDER S. SZALAY  
Department of Physics and Astronomy, Johns Hopkins University, 3400 N Charles St, Baltimore, MD 21218  
*Draft version November 1, 2018*

### ABSTRACT

We present the ORIGAMI method of identifying structures, particularly halos, in cosmological  $N$ -body simulations. Structure formation can be thought of as the folding of an initially flat three-dimensional manifold in six-dimensional phase space. ORIGAMI finds the outer folds that delineate these structures. Halo particles are identified as those that have undergone shell-crossing along 3 orthogonal axes, providing a dynamical definition of halo regions that is independent of density. ORIGAMI also identifies other morphological structures: particles that have undergone shell-crossing along 2, 1, or 0 orthogonal axes correspond to filaments, walls, and voids respectively. We compare this method to a standard Friends-of-Friends halo-finding algorithm and find that ORIGAMI halos are somewhat larger, more diffuse, and less spherical, though the global properties of ORIGAMI halos are in good agreement with other modern halo-finding algorithms.

*Subject headings:* dark matter – galaxies: halos – large-scale structure of Universe – methods: numerical

### 1. INTRODUCTION

Cosmological  $N$ -body simulations allow one to calculate the time-evolution of an initial density field, discretized as a set of dark matter point particles with a given mass, from the distant past when the field was quite smooth to the present-day hierarchy of halos, filaments, walls, and voids. Identifying these structures remains one of the key challenges to the process of comparing these simulations to observations of galaxies and clusters. Though some efforts have been made to identify complex structures such as filaments and walls (Aragón-Calvo et al. 2007; Hahn et al. 2007; Forero-Romero et al. 2009; Bond et al. 2010; Shandarin 2011), most of the focus is on identifying the dark matter halos in which galaxies reside or the voids that comprise most of the cosmological volume.

The two best-known ways of identifying halos in simulations are the Spherical Overdensity (SO, Press & Schechter 1974; Lacey & Cole 1994) and Friends of Friends (FOF, Davis et al. 1985) methods. Since these were developed, the number of halo-finding algorithms has grown quite large (for an extensive listing, see Knebe et al. 2011, and references therein), but many of these modern methods rely at their core on the SO (e.g., Klypin & Holtzman 1997; Knollmann & Knebe 2009; Planelles & Quilis 2010; Sutter & Ricker 2010) or FOF (e.g., Gottlöber et al. 1999; Springel et al. 2001; Gardner et al. 2007; Habib et al. 2009; Rasera et al. 2010) algorithms. Other methods work in phase-space (Diemand et al. 2006; Maciejewski et al. 2009; Behroozi et al. 2011; Elahi et al. 2011), or in some other way group particles around density peaks (Eisenstein & Hut 1998; Stadel 2001; Aubert et al. 2004; Neyrinck et al. 2005; Tweed et al. 2009). In detail, these methods differ in terms of how densities are calculated, whether they perform any post-processing or “unbinding” procedures, whether they identify sub-structures, and implementation details such as code parallelization. Recently the “Haloes Gone

MAD” comparison project has tested many of these methods on an equal footing, finding that the differences for the basic halo properties in a cosmological simulation are well within the expected error (Knebe et al. 2011).

We would like to note, however, that the agreement between different halo-finding methods for only the most massive halos, or for masses defined within some radius, is perhaps not unexpected, since one of the largest sources of variation between methods is the definition of the halo boundary or outer-edge. Often this is because the halo boundary depends quite strongly on the value of a free parameter in the algorithm, such as a density cut-off or (in the case of FOF) a linking length that effectively serves as a proxy for density (Eisenstein & Hut 1998; Neyrinck et al. 2005; Knebe et al. 2011; Anderhalden & Diemand 2011). Knebe et al. (2011) did not explicitly test the agreement among halo finders of halo boundaries, for which we expect a criterion could be designed that would show surprisingly poor agreement, such as the maximum Cartesian halo size which we use below. Going to full six-dimensional phase-space (Diemand et al. 2006; Maciejewski et al. 2009; Knebe et al. 2011; Behroozi et al. 2011) allows impressive identification of distinct halo subhalo cores (as well as streams), although even here the boundaries of halos and subhalos can be ambiguous. As pointed out by Shandarin et al. (2012), knowledge of the initial and final conditions of position coordinates is equivalent to knowledge of the full six-dimensional phase space in the final conditions for a classical Hamiltonian system, a fact which we exploit.

In this paper, we present the ORIGAMI<sup>1</sup> structure-finding algorithm which finds halos by testing whether particles have undergone shell-crossing. We set halo boundaries at their outer caustic, i.e. at the outermost phase-space fold, which Zukin & Bertschinger (2010)

<sup>1</sup>

have found to correspond well in an analytical model to a conventional density-based concept of a virial radius. The formation of structures in the universe has long been linked to the formation of caustics as matter piles up and forms pancakes or sheets (Zel’dovich 1970; Peebles 1980, p. 95). These caustics mark out the boundaries of multi-stream regions, i.e., locations in physical space for which the velocity field is multi-valued. Particles that have entered multi-stream regions are said to have undergone shell-crossing, and their dynamics become quite complicated as they settle into a bound structure (Kofman et al. 1990, 1992; Vogelsberger et al. 2008; White & Vogelsberger 2009; Shandarin 2011; Valageas 2011; Vogelsberger & White 2011).

To provide some intuition as to how the ORIGAMI method works, consider that though usually particles are thought of as simple blobs of mass, they can also be thought of as vertices of an initially regular grid (which is often the case for the initial conditions of  $N$ -body simulations; however, ORIGAMI currently does not work for “glass-like” initial conditions). Gravity distorts this grid, causing some of its cells to collapse and invert when shell-crossing structures form. In three-dimensional position space, in such shell-crossing regions, multiple cells overlap at the same position.

However, in six-dimensional phase space, these cells never cross, assuming a numerical-error-free simulation of collisionless dark matter. Instead, a three-dimensional manifold, or sheet, stretches and folds in six dimensions, forming familiar large-scale structures when the velocity coordinates are projected out. Extrapolating to time zero, the grid is exactly regular in position coordinates and all velocities are zero, so initially this sheet is flat in phase space. Then in subsequent gravitational evolution, the sheet folds without intersecting itself in phase space. If there were such an intersection, then two dark-matter particles with different initial coordinates would have the same phase-space coordinates at a later time, a contradiction for a Hamiltonian dynamical system (Landau & Lifshitz 1969). This picture has also recently been explored by Shandarin et al. (2012) and Abel et al. (2011). They use tetrahedral tessellations on the initial grid to identify shell crossings. Abel et al. (2011) use this to measure densities within the phase-space sheet, allowing for example a particularly clean visualization of the cosmic web. Our framework, however, keeps track of the number of axes along which particles have crossed, enabling structures to be classified as voids, walls, filaments and halos.

Figure 1 illustrates the wrapping and stretching that gravity imparts to an initially flat sheet of particles in phase space. We plot two projections of a Lagrangian sheet of  $256^2$  particles from a full 3D  $256^3$ -particle cosmological simulation run to redshift zero. The bottom sheet projects out the velocity coordinates and shows the familiar  $(x, y, z)$  coordinates. The top sheet offers a peek into velocity space, replacing the  $z$  (vertical) coordinate with  $v_x/H_0$ , the  $x$  (horizontal) component of the velocity scaled with the Hubble constant. Halos are visible as knots in the bottom sheet; in the top sheet, they show up as furious spikes, which if zoomed into would ideally exhibit a spiral structure (e.g., Fillmore & Goldreich 1984; Bertschinger 1985; Widrow & Kaiser 1993).

Implicit in the name of our algorithm is an analogy to origami. In cosmological structure formation, as in origami, the “sheet” starts out flat initially, and never crosses itself when viewed in phase space. But of course, the analogy is not complete. Cosmological sheets stretch, unlike origami sheets. Also, the dimensionality is different: the folding of an actual two-dimensional origami sheet occurs in three dimensions, whereas even in a two-dimensional universe, folding of the cosmological sheet occurs in four dimensions. If we flatten away the velocity coordinates, the situation is analogous to “flat origami,” a restriction of origami in which the end result of the folding is constrained to lie flat in a plane. In the cosmological case, dark-matter caustics correspond to creases in the folded structure. The field of flat origami has been studied mathematically (e.g. Hull 1994; Lang 1996; Hull 2002, 2006), and in the discussion section we speculate on some applications of those results to large-scale structure.

We describe the ORIGAMI method in Section 2, including how particles are tagged according to their morphology, how these particles are grouped into halos, and how halo properties are calculated. Our morphology classification results are given in Section 3.1. In Section 3.2 we compare the ORIGAMI halo catalog to a standard FOF catalog, and in Section 3.3 we study the effects of the mass resolution of the simulation. Finally, we discuss particular features and speculate on potential applications of ORIGAMI in Section 4, and we give concluding remarks in Section 5.

## 2. METHOD

Most fundamentally, the ORIGAMI algorithm classifies particles according to their morphological structure into void, wall, filament, and halo particles, which we describe in Section 2.1. Usually, a catalog of structures is desired, which requires grouping these particles. There are many ways to do this, and we explain our procedure, based on a Voronoi tessellation in Eulerian space, in Section 2.2. Finally, we describe our method of measuring halo properties in Section 2.3, which will be used to compare halo catalogs in the following sections.

### 2.1. Morphology Classification

ORIGAMI classifies the morphologies of particles based on the number of orthogonal directions along which the Lagrangian “origami” phase-space sheet is folded. Although the origami-folding occurs in full phase space, for the present paper we make use only of position space, taking advantage of the fact that the relative positions of particles within folded regions have been reversed with respect to the initial grid. It may help for some purposes (such as demarcating subhalos) to include velocity information as well; however, as mentioned above, knowledge of the initial and final states of a classical Hamiltonian system is equivalent to knowledge of the final positions and velocities. The initial state for a cosmological simulation run from an initial particle lattice is particularly simple and thus a natural choice of data to exploit.

A particle’s ORIGAMI morphology is determined by the number of axes along which particle-crossing has occurred. In one dimension, this is trivially tested by determining whether the final (Eulerian) positions of two

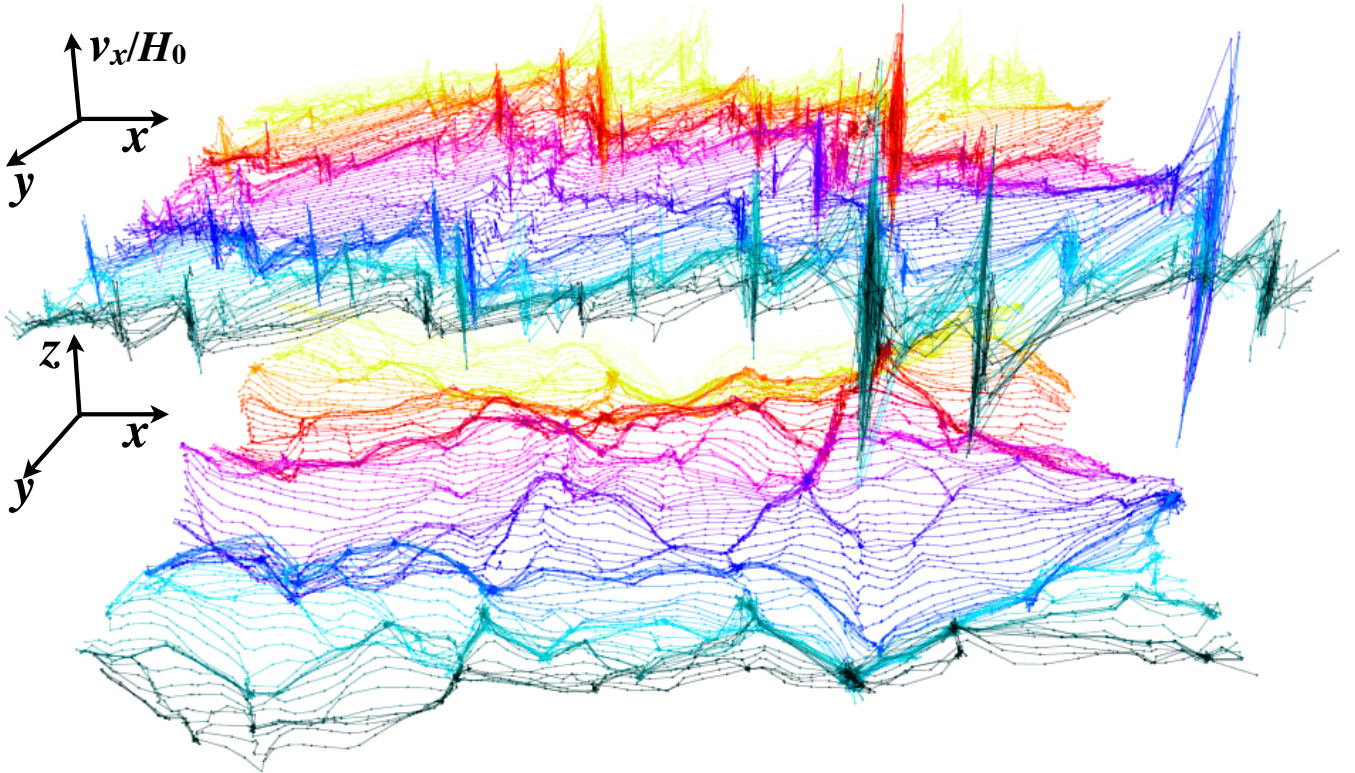


**Figure 1.** Distortion and folding in phase-space at the present epoch of a  $128^2$ -particle sheet, roughly  $100 h^{-1}$  Mpc on a side. This is a quarter of a  $256^2$ -particle sheet, initially a two-dimensional flat slice through the  $256^3$ -particle cubic lattice. In the bottom sheet, particles are plotted at their familiar position coordinates,  $(x, y, z)$ ; in the top sheet, the  $z$  coordinate switches to  $v_x/H_0$ , the  $x$ -component of the velocity scaled with the Hubble constant. Rows of particles are colored according to their initial (Lagrangian)  $y$ -coordinate.

particles are out of order with respect to their initial (Lagrangian) positions. This means that if we index the particles according to their positions on the initial, regular Lagrangian lattice, particles  $i$  and  $j$  have crossed if  $i < j$  but their order along that axis is swapped, i.e. their Eulerian positions  $x_i > x_j$ . In two or three dimensions, we use this same criterion to detect crossings along rows and columns of the initial Lagrangian lattice. A particle  $i$  has been crossed along the  $x$  axis if there exists a particle  $j$  in its initial  $x$ -oriented row such that  $(x_i - x_j)$  and  $(i - j)$  have opposite signs, where again the indices  $i$  and  $j$  increase with initial  $x$ -coordinate. Note that we are taking advantage of the lack of substantial vorticity on cosmological scales; if a region in a simulation were able to rotate along three axes, our algorithm would detect that as well.

Void, wall, filament, and halo particles are particles that have been crossed along 0, 1, 2, and 3 orthogonal axes, respectively. This number is a particle’s ORIGAMI morphology index  $M$ . The most natural set of axes to use is the intrinsic Cartesian  $x$ ,  $y$ , and  $z$  axes of the initial grid, but particle crossing may occur along other axes as well. In practice, using only the Cartesian axes seemed to detect only about half of the particle crossings, in the sense that sets of halo particles that should have been contiguous (see Figure 4 below) contained non-halo particles. We found that using three additional orthogonal triplets of axes filled these holes. Each triplet consists of one intrinsic  $x$ ,  $y$ , or  $z$  axis and two  $45^\circ$ -diagonal axes in the plane perpendicular to the intrinsic axis. The mor-

phology index  $M$  returned is the maximum  $M$  among all four sets of axes.

In principle, there is a huge number of “higher-order” axes along which particles might cross, which are at odd angles with respect to the Cartesian grid. As the “order” of a set of axes increases, so does its minimum initial particle separation (if a cubic initial grid is used). This increased particle separation decreases the likelihood that particles along these axes will interact and collapse into the same bound structure. Figure 2 shows a schematic of the initial particle separation along different choices of axes (here in two dimensions for clarity), including the Cartesian grid, axes rotated by  $45^\circ$ , and a “higher-order” set of axes. Note that the initial particle separation is not the same along each axis for these rotated sets of axes, a property which is quite rare and leads to even larger initial separations.

We find that including particle-crossings detected along all 6 permutations of the extra set of axes shown in Figure 2 increases the number of halo particles by only 3% or 4% (depending on simulation resolution), and in all, only about 5% of particles increase their morphology index  $M$ . These added particles have a negligible effect on the halo mass functions and a small effect on the halo sizes (defined in Section 2.3), growing the halos slightly. Though in principle many more higher-order axes could be used to find particle-crossings, these added particles do not change our conclusions while adding significant computational time to the morphology classification, so using only the 4 lowest-order sets of axes to determine

ORIGAMI morphology provides a good balance between strict completeness and computational efficiency.

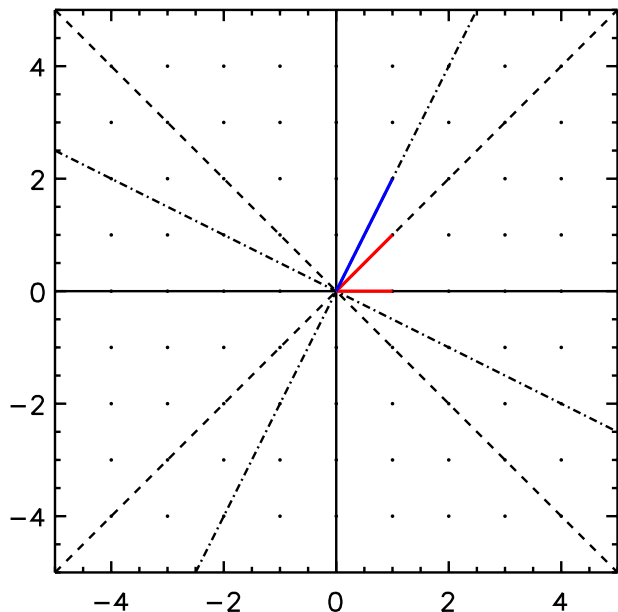


**Figure 2.** Schematic of the initial particle separation along different sets of axes. The Cartesian axes (*solid*) and a  $45^\circ$  diagonally-rotated set of axes (*dashed*) have the smallest particle separations (shown in *red*). A third set of axes (*dot-dashed*) has the next-largest particle separation (shown in *blue*). We use the Cartesian grid and the three sets of  $45^\circ$  rotated axes (where the rotation is in the  $x$ - $y$ ,  $y$ - $z$ , and  $x$ - $z$  planes) to test for particle crossing.

The particle-crossing detection algorithm is simple and very fast. For each particle, for all six axes ( $x$ ,  $y$ ,  $z$ , and the  $45^\circ$ -diagonal axes in the  $x$ - $y$ ,  $y$ - $z$ , and  $x$ - $z$  planes), we march forward (not backward, since all particles are tested) along the initial lattice and test for any crossing along that axis. Denoting the number of particles in an initial row or column as  $N_{1D}$ , we test up to  $N_{1D}/4$  particles in each row, i.e. proceeding along  $1/4$  of the initial lattice and stopping early if a crossing-detection occurs. We do not approach  $1/2$  of the lattice, since at that separation a false detection could occur as an artifact of periodic boundary conditions (PBC). Thus the number of distance tests required, in worst case (when a full fourth of a row is tested for each particle) is  $2 \times 6N_{1D}N/4 = 3N^{4/3}$ , where the total number of particles in the simulation is  $N = N_{1D}^3$ . The factor of 2 is from distance tests from PBC-corrections, and the factor of 6 is from the total number of axes tested.

ORIGAMI morphology can be determined at any of the output redshifts of the simulation, but we only use the positions at that redshift to test for particle-crossing. This means that if particles have crossed at an earlier redshift, we do not use that information but instead look for new particle-crossings. We leave the study of redshift-dependent ORIGAMI morphology, for example whether it will aid in substructure identification, to future work; however, we note that retaining the ORIGAMI morphology of the next-to-last snapshot (i.e. not allowing  $M$  to decrease) increases the number of  $z = 0$  halo particles by a few percent. In Section 3 we present the morphology

results and halo catalogs using  $z = 0$  only.

## 2.2. Grouping Halo Particles

Once all particles have been given a morphology classification, we group the halo particles using a Voronoi/Delaunay tessellation, which provides a natural density estimate (Voronoi Tessellation Field Estimator (VTFE), Schaap & van de Weygaert 2000; van de Weygaert & Schaap 2009) and set of neighbors for each particle. A Voronoi tessellation partitions space into cells, such that all points inside a particle’s Voronoi cell are closer to that particle than to any other. The Delaunay tessellation is the dual of the Voronoi tessellation and divides a 3-dimensional volume into a set of tetrahedra (or a 2-dimensional area into triangles) that connect particles, such that the particles in two adjacent Voronoi cells are connected in the Delaunay tessellation. The VTFE density at each particle is given by  $\delta_{VTFE} = \bar{V}/V - 1$ , where  $V$  is the particle’s Voronoi cell volume and  $\bar{V}$  is the average of  $V$  among all particles.

We group halo particles that are connected on the Delaunay tessellation, but to prevent long strings of halos from being linked, we first require that halos contain only one “core” or set of connected halo particles above some VTFE density threshold. This becomes the only parameter in the ORIGAMI algorithm, which we set to 200 times the mean density. In this first round, any particles meeting this criterion that are Delaunay neighbors are given the same halo ID. We then add the lower-density halo particles that are connected to the halo cores by iteratively adding Delaunay neighbors until all connected particles are associated. Finally, we group any leftover halo particles that are not connected to a core but are connected to each other on the tessellation.

We find that the core density threshold has a small effect on the mass functions of the grouped halos and has negligible effect on the distribution of halo sizes (defined in Section 2.3). The effect on the mass function is shown in Figure 3. A smaller threshold produces fewer small halos and a higher threshold leads to more small halos, as might be expected. The differences in the cumulative mass functions for  $\rho_{cut} = 150$  and  $\rho_{cut} = 250$  are within the 10% level compared to the value of  $\rho_{cut} = 200$  used throughout the paper, and they are smaller than the difference with FOF. See Section 3.2 for more discussion of ORIGAMI vs. FOF mass functions.

The grouping procedure thus puts all of the tagged halo particles into individual halos. Since the tagging procedure establishes halo boundaries by identifying halo particles, no post-processing to remove unbound particles is performed. In principle, there is no lower limit to the number of particles in an ORIGAMI halo, though it is hard to imagine isolated particles being classified as a halo as described above. However, we require that halos contain at least 20 particles in order to be included in our final catalog.

## 2.3. Measuring Halo Properties

In this section we define the halo properties used to compare halo catalogs in Sections 3.2 and 3.3. These will be used to calculate the halo properties for both



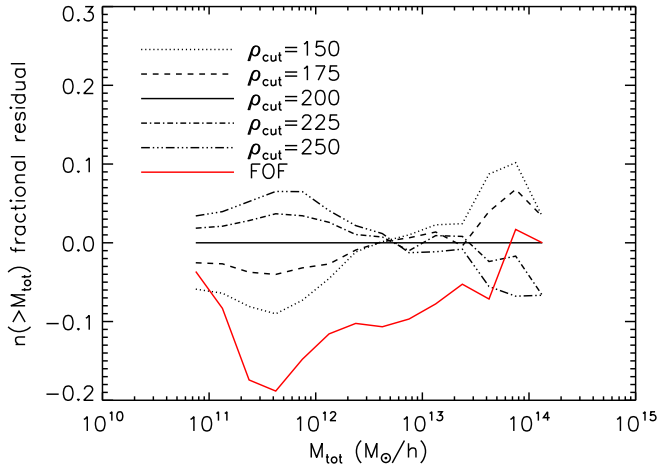


**Figure 3.** The effect of different values for the “core” density threshold shown as fractional residuals from the cumulative mass function of the  $\rho_{cut} = 200$  value used throughout the paper. Relaxing this value produces fewer small halos, and increasing it produces more small halos, though the difference is small.

the ORIGAMI and FOF halo catalogs. One of the most important is the definition of the halo center, since it affects many other calculated properties. We define the center to be the average position of the halo particles, weighted by their VTFE density. This greatly reduces the dependence of the location of the center (and many halo properties) on the low-density outer regions of non-spherical halos, compared to a non-weighted average.

We determine  $R_{200}$ , the radius beyond which the density drops below 200 times the critical density ( $\rho_{crit}$ ), and  $M_{200}$ , the mass within this radius, by sorting the particles according to their radius from the halo center and determining the maximum radius for which the density within this radius is greater than  $200\rho_{crit}$ . If no radius meets this criterion for a specific halo, we consider  $R_{200}$  and  $M_{200}$  undefined and set their values to zero. We look at mass functions of  $M_{200}$ , which is a common definition of halo mass found in the literature (see, e.g., Knebe et al. 2011).

Though  $M_{200}$  is commonly used to define the mass of halos, we also look at the total mass of all halo particles in order to include the full extent of the halo, since one of the key differences of ORIGAMI compared to other methods is its dynamical definition of the halo boundary. Knebe et al. (2011) found that  $v_{max}$ , the peak of the rotation curve, is a stabler definition of halo mass across different halo finders, but this is also due largely to its insensitivity to halo boundaries. We use the more discriminating total mass of a halo in our comparisons, since a major motivation for our algorithm is to create an objective definition of the halo boundary.

The final property we will compare is the halo size, which we define as the maximum diameter along the Cartesian  $x$ ,  $y$ , and  $z$  directions. This choice is preferred to other common measures such as  $R_{200}$  because it captures the outer regions of the halo. The halo size is calculated in the following way: first we transform the halo particle positions to a local coordinate system to account for PBC; we then calculate  $s_x = \max(x) - \min(x)$  for the  $x$ ,  $y$ , and  $z$  coordinates; and finally we take the halo size to be the maximum of  $(s_x, s_y, s_z)$ . We choose

this definition over, for example, the maximum radius of the particles in the halo because it does not depend on the definition of the halo center.

### 3. RESULTS

We first present the morphology classification that ORIGAMI gives to particles in an  $N$ -body simulation in Section 3.1. We then focus on comparing ORIGAMI to FOF in Section 3.2, followed by an investigation of the effects of resolution on both ORIGAMI and FOF catalogs in Section 3.3.

#### 3.1. Morphology

In this section we use a  $256^3$ -particle simulation with a box size of  $200 h^{-1}\text{Mpc}$  and standard  $\Lambda\text{CDM}$  cosmology ( $h = 0.73$ ,  $\Omega_M = 0.3$ ,  $\Omega_\Lambda = 0.7$ ,  $n_s = 1$ , and  $\sigma_8 = 0.9$ ). The results of the ORIGAMI morphology classification described in Section 2.1 are shown, for a slice through the simulation box, in Figure 4. The middle panel shows, in Lagrangian coordinates, the redshift-zero ORIGAMI morphology indices  $M$  of  $256^2$  particles that inhabit a flat plane with equal  $z$  in the initial lattice. Each pixel of the square image corresponds to a particle. The bottom panel shows the particles in Eulerian coordinates, again colored according to  $M$ .

The top panel of Figure 4, plotted in Lagrangian space, shows the VTFE density (described in Section 2.2) at each particle. The color scale is logarithmic, and a faint red contour is added at  $1 + \delta_{\text{VTFE}} = 61$ . This density, perhaps surprisingly low, divides halo from non-halo particles if one (wrongly) assumes that “haloness” depends only on density. More precisely, the fraction of particles exceeding this density equals the fraction of particles that are ORIGAMI-identified halo particles. Figure 5 shows the four morphological components of the bottom panel of Figure 4, separated out for clarity.

In these figures, the ORIGAMI identification of particle morphologies accords with expectation, most obviously for void and halo particles. For wall and filament particles, the situation is harder to assess in a two-dimensional image, but again the classification looks reasonable. A couple of small regions appear void-like in this two-dimensional projection and yet are classified as walls; the shell-crossings producing these walls happen to lie in the plane of the figure. A comparison of ORIGAMI morphology to other morphology measures will be the subject of a future study.

There is an interesting duality between the structures in the middle and bottom panels of Figure 4. This duality was noticed by investigators of the adhesion model of structure formation (e.g., Kofman et al. 1990, 1992). Halos in Lagrangian space are large bubbles that are qualitatively like voids in Eulerian space, although Eulerian voids are more polyhedral, whereas Lagrangian halos are generally rounder. Dually, voids in Lagrangian space are small, as are halos in Eulerian space. The situation with filaments and walls is harder to see, but in Figure 4 many Eulerian filaments look, in Lagrangian space, like walls dividing bubbles (halos).

#### 3.2. Comparison to Friends-Of-Friends

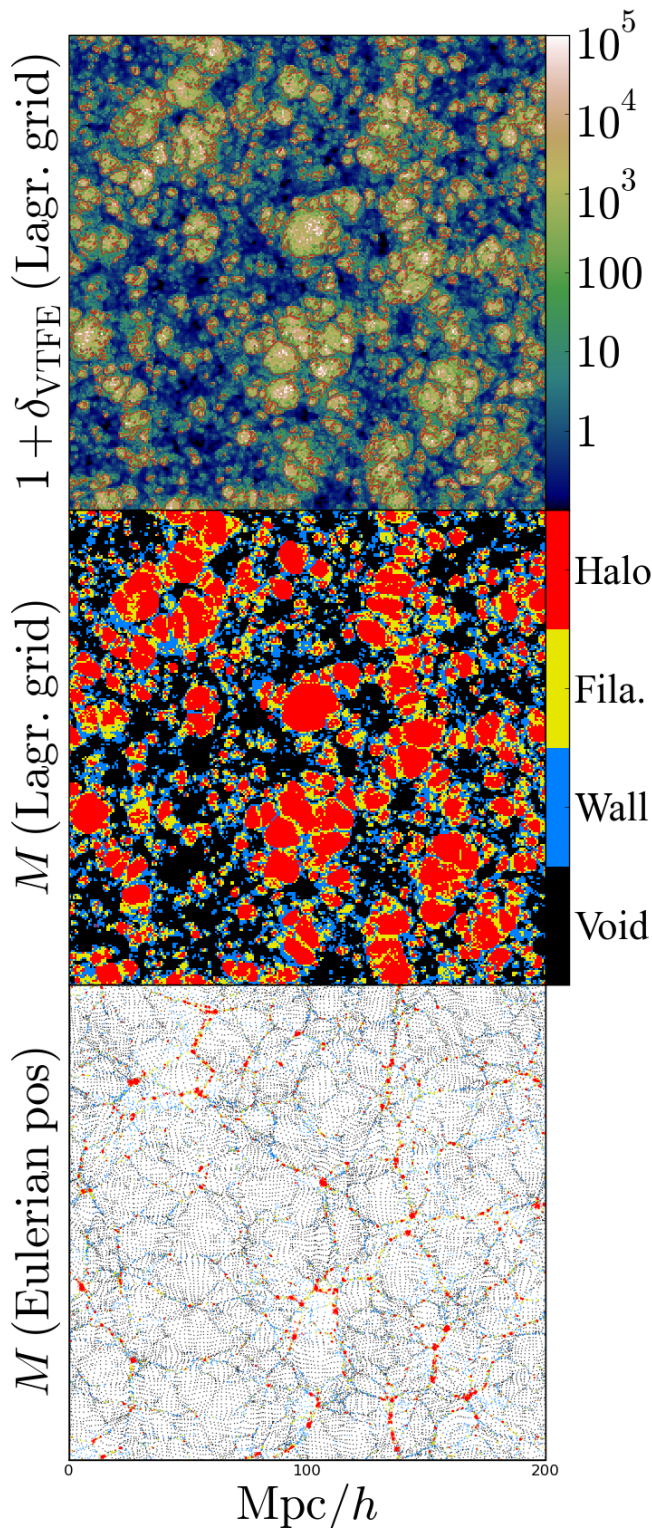


**Figure 4.** Redshift-zero quantities measured from a  $256^2$  sheet of particles that share the same  $z$ -coordinate in the initial-conditions lattice. The top two panels are shown in Lagrangian coordinates, in which each particle is a pixel in a  $256^2$  image. *Top:* Voronoi-tessellation density estimates, at each particle (see text for explanation). A red contour is drawn at  $1 + \delta = 61$  (see text for details). *Middle:* ORIGAMI morphology indices  $M$ . *Bottom:* Here the  $M$ -colored particles (0-3 are shown in black, blue, yellow, and red) are plotted at their  $(x, y)$  Eulerian coordinates.

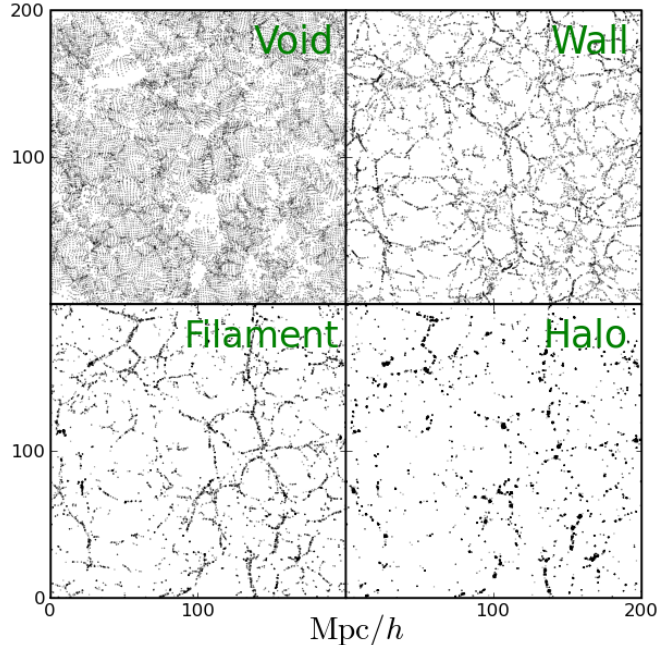


**Figure 5.** The four components of the bottom panel of Figure 4, separated into different panels.

As part of the “Haloes Gone MAD” comparison project (Knebe et al. 2011), ORIGAMI has been shown to be in general agreement with most of the standard halo-finders in use today. To look at the details of how ORIGAMI works, particularly in the limit of very small halos where methods tend to disagree the most, we create ORIGAMI and FOF catalogs for a  $100 h^{-1} \text{Mpc}$   $N$ -body simulation with similar cosmology parameters as above (except  $n_s = 0.93$  and  $\sigma_8 = 0.81$ ) and at two different mass resolutions. The high-resolution simulation has  $512^3$  particles and will be referred to in what follows as the 512 simulation. The low-resolution simulation has  $256^3$  particles with initial conditions down-sampled from the 512 simulation, such that the only difference between the initial density fields of the two simulations is the resolution, and it will be referred to as the 256 simulation.

The FOF halo-finding method is one of the most widely-used and well-understood halo finders. It works by connecting particles that are separated by a distance smaller than some linking length, which is a parameter that we set to the typical value of 0.2 times the mean inter-particle separation. Though popular, FOF is not without issues. As noted widely in the literature, this method of linking particles into halos causes some fraction of the halos to be “bridged” such that two density peaks connected by a filament of particles are grouped into the same halo (see, e.g., Lukić et al. 2009). Additionally, there is some doubt as to whether FOF captures the full amount of particles involved in the collapse of the halo (Anderhalden & Diemand 2011). This issue of the definition of halo edges is partly what motivated Knebe et al. (2011) to prefer  $v_{\text{max}}$  as a stable quantity by which to compare halo catalogs, as it largely ignores the outer parts of halos.

We first compare the cumulative mass functions. There is good agreement between ORIGAMI and FOF in the to-

tal mass (Figure 6), with ORIGAMI finding more very low mass halos (especially for the 512 simulation; see Section 3.3) and FOF finding slightly more very high mass halos. This situation changes when considering  $M_{200}$  (Figure 7); ORIGAMI finds fewer low mass halos, as noticed in Knebe et al. (2011), when this definition of the halo mass is used. This is because there are many more ORIGAMI halos that do not have a defined  $M_{200}$ , having no radius for which the density is greater than  $200\rho_{crit}$  (as described in Section 2.3). This is largely due to ORIGAMI halos being in general more diffuse and non-spherical than FOF halos and therefore more sensitive to the location of the halo center. As seen in Table 1, ORIGAMI starts with more halos than FOF at both resolutions – and even more considering halos with fewer than 20 particles, though we do not consider them here – but ORIGAMI loses a much higher percentage of its halos when counting only those that have a defined  $M_{200}$ .

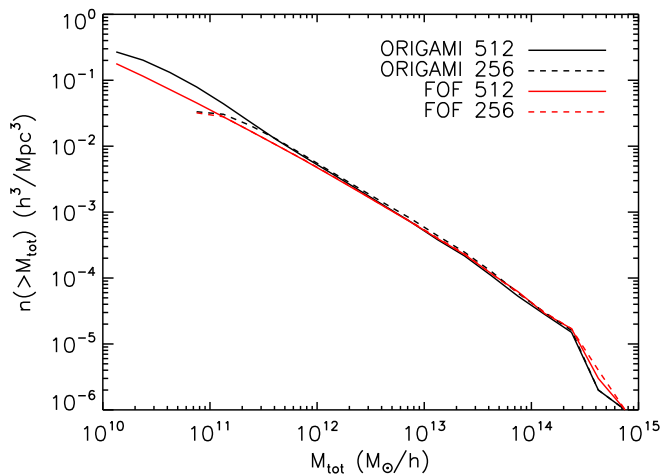


**Figure 6.** Cumulative distribution functions of total mass for ORIGAMI and FOF halos at both mass resolutions.

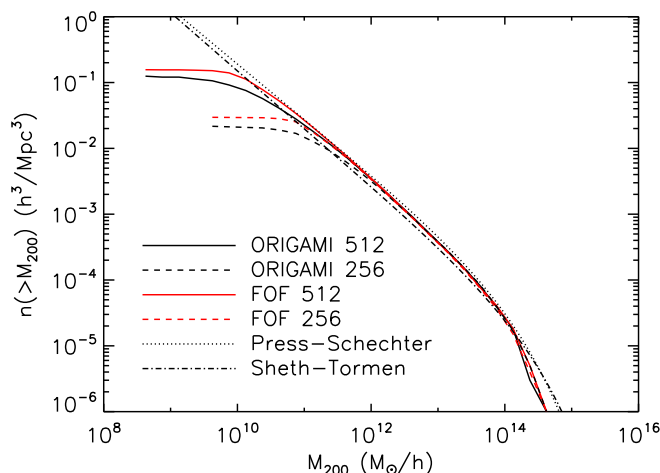


**Figure 7.** Cumulative distribution functions of  $M_{200}$  for ORIGAMI and FOF halos at both mass resolutions. The theoretical curves of Sheth & Tormen (1999) and Press & Schechter (1974) are plotted for reference and are in good agreement.

We now turn to the distributions of halo size, defined as the maximum Cartesian diameter in Section 2.3, and find that ORIGAMI and FOF have very different distri-

**Table 1**  
Number of halos  $N_h$  for different halo-finders and simulation resolutions

Halo-finder	Sim.	$N_h$ ( $\geq 20$ particles)	$N_h$ (defined $M_{200}$ )
ORIGAMI	256	33266	21632
FOF	256	32052	29612
ORIGAMI	512	269192	124870
FOF	512	178397	156686

butions (Figure 8). For the 256 simulation, FOF halos have a distribution around  $0.3 h^{-1}\text{Mpc}$  while ORIGAMI halos have a slightly wider distribution with a mean of around  $0.7 h^{-1}\text{Mpc}$ . Since the total mass functions are similar, it appears that ORIGAMI halos are more diffuse and extend beyond the outer boundaries of FOF halos (which may be missing these edge particles (Anderhalden & Diemand 2011)), while at the same time ORIGAMI halos sometimes (though not often) contain within them non-halo particles tagged with  $M = 2$  (filament) instead of  $M = 3$  (halo; see Section 2.1). Recall that no unbinding procedure has been performed on either halo catalog, which would potentially remove the unbound particles from FOF halos, similar to how the interloping  $M = 2$  particles are ignored in the ORIGAMI method.

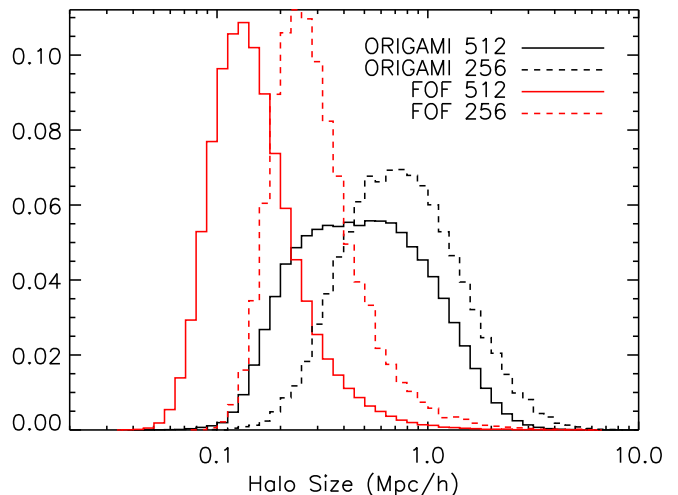


**Figure 8.** Distribution of halo sizes (defined as the maximal diameter among Cartesian directions) for ORIGAMI and FOF halos at both mass resolutions.

The other effect causing the difference in halo sizes is that the very small FOF halos often contain a mix of  $M = 2$  and  $M = 3$  particles, such that fewer than 20  $M = 3$  particles are grouped and therefore the group does not make it into the ORIGAMI halo catalog. This can be seen in Fig. 9, where a small region of the simulation containing one ORIGAMI halo and a few small FOF halos is plotted showing FOF halo particles in red, ORIGAMI halo particles (in which halos have at least 20 particles) in purple, and ORIGAMI-classified  $M = 3$  particles in green. Though some  $M = 2$  particles are close enough to their  $M = 3$  neighbors to be grouped by the FOF method, they do not meet the ORIGAMI definition of a halo particle.

The VTFE density distributions for FOF and ORIGAMI particles are shown in Figure 10 for the 256 simulation. There is a more abrupt distinction between halo and non-



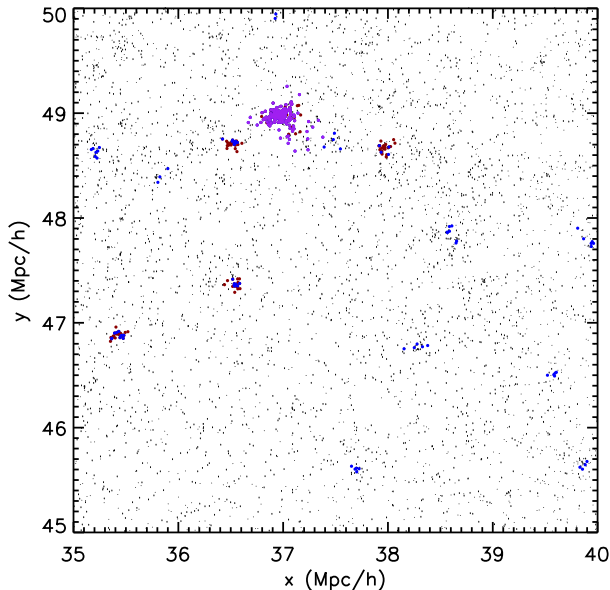


**Figure 9.** Particle locations in a  $5 \times 5 h^{-1} \text{Mpc}$  region of the 256 simulation,  $40 h^{-1} \text{Mpc}$  deep in the  $z$ -direction. Over-plotted as larger dots are FOF halo particles in *red*,  $M = 3$  halo-classified particles in *blue*, and lastly ORIGAMI halo particles (with at least 20 particles per halo) in *purple*. The small FOF halos contain some, but fewer than 20,  $M = 3$  particles, and so do not become ORIGAMI halos.

halo particles for the FOF distributions than there is for the ORIGAMI distributions, which accords with the common conception that the FOF linking length parameter corresponds to a density (but for a detailed study of this issue see More et al. 2011). It is interesting here to note that the double-peaked histogram of  $\log(1 + \delta_{\text{VTFE}})$  is a particular feature of the mass-weighted nature of the density calculated from the Voronoi tessellation. As mass resolution increases and more small-scale features are resolved in a simulation, this peak grows (see, e.g., Fig. 14 in Section 3.3), whereas an Eulerian (volume-weighted) measure of the density would wash out these features.

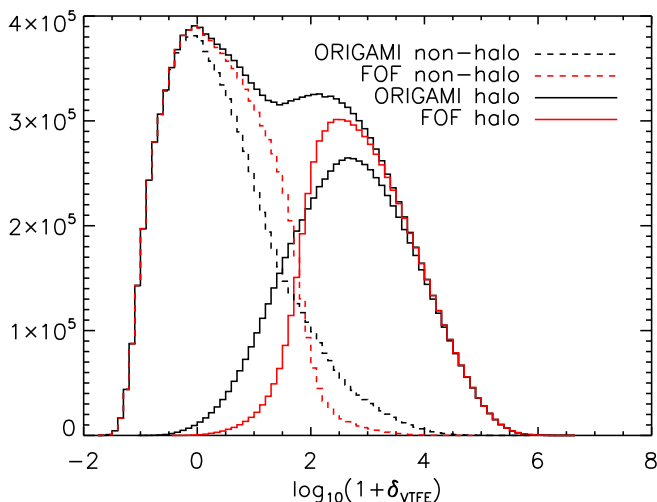


**Figure 10.** Distribution functions of the VTFE particle density for FOF and ORIGAMI halo and non-halo particles from the 256 simulation.

In Figure 11 the VTFE density distributions are plotted for ORIGAMI particles separately based on morphology tag. As expected, the morphology tag is correlated with density, though there is much overlap, and in particular the  $M = 2$  particles have a long tail out to high densities. This tail likely corresponds to  $M = 2$  particles clustered near  $M = 3$  particles that become (small) FOF halos but contain too few  $M = 3$  particles to become ORIGAMI halos (see Fig. 9).

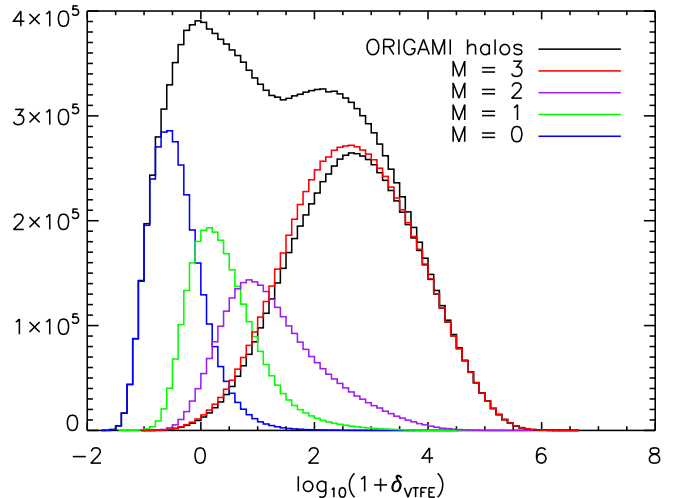


**Figure 11.** Distribution functions of the VTFE density for particles tagged as  $M = 0$  (void, blue),  $M = 1$  (wall, green),  $M = 2$  (filament, purple), and  $M = 3$  (halo, red), for the  $N = 256$  simulation. The distribution function for ORIGAMI halos is different than that for the  $M = 3$  particles because of the requirement that halos contain at least 20 particles.

### 3.3. Resolution Effects

In general, we expect that as resolution increases, the boundaries of large halos remain fairly constant and new, smaller halos with lower masses are identified. Indeed, this is what ORIGAMI finds, as shown in Figure 12, which shows the ORIGAMI morphologies of the same redshift-zero Lagrangian sheet in the 256 and the 512 simulations. Recall that the 256 simulation is the same as the 512 simulation, but with coarsened resolution on the initial grid. New halo regions appear in the 512 simulation, particularly in void and wall regions of the 256 simulation.

However, the effect of resolution does not appear to be quite the same for the ORIGAMI and FOF halo catalogs. As noted in Section 3.2, the difference between the ORIGAMI and FOF cumulative total mass functions is much greater for the 512 simulation than for the 256 simulation (see Figure 6), with ORIGAMI finding noticeably more low mass halos. This means that the effect of increasing the simulation resolution adds many more ORIGAMI halos than FOF halos. This effect is not seen in the  $M_{200}$  mass function (Figure 7) because these smaller halos continue to have an undefined  $M_{200}$ , and so the effect of increased resolution for both catalogs is the extension of the  $M_{200}$  mass function down to lower masses.

The reason why there are many more low mass halos in the 512 simulation is because a greater percentage of particles (56.6%) are tagged as  $M = 3$  halo particles,



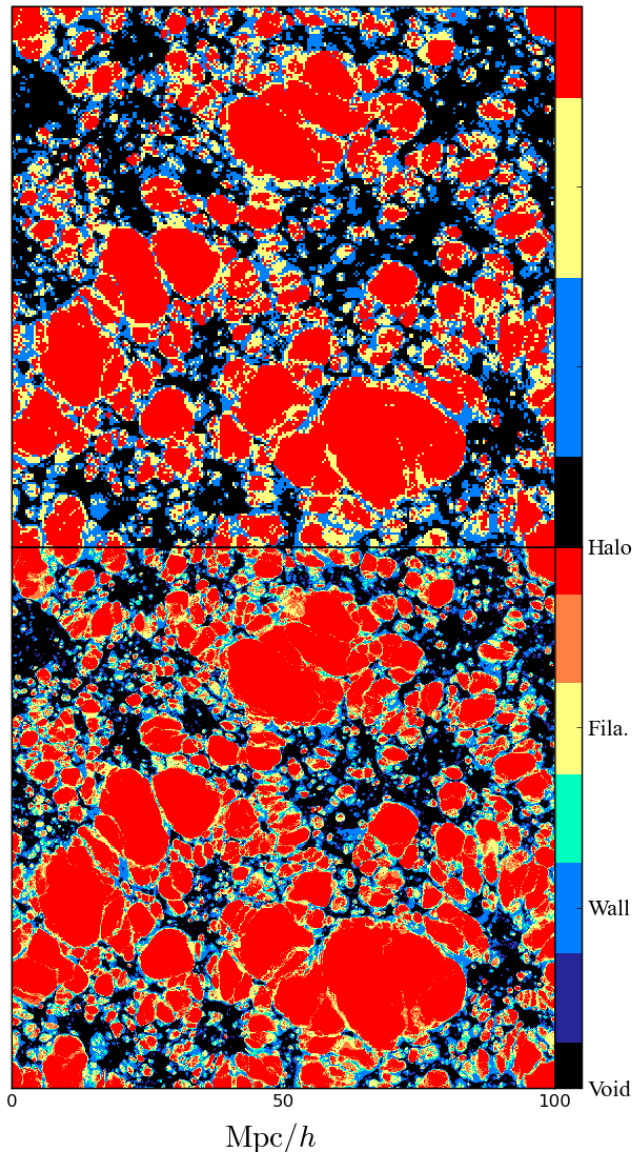


**Figure 12.** The ORIGAMI morphologies  $M$ , shown in Lagrangian coordinates, of initially two-dimensional sheets of particles in the 256 (*top*) and 512 (*bottom*) simulations. In the top panel, each of the  $256^2$  pixels corresponds to a particle. In the bottom panel, the  $512^2$  pixels are colored according to the average ORIGAMI morphologies of the two  $512^2$  sheets that comprise the  $256^2$  sheet in the top panel. Half-integers occur in the bottom panel because of this averaging. For clarity, we show a slice with a relatively small fraction of halo particles.

compared to 47.7% in the 256 simulation. This is partially related to the greater percentage of high density particles in the 512 simulation in general, as shown in Figure 13, compared to the 256 simulation in Figure 11. This increase in density also affects the FOF halo catalog, however it is to a much lesser degree: 47.3% of particles are in FOF halos in the 512 simulation, compared to 42.7% in the 256 simulation (see Figure 14).

If we look again at the distribution of halo sizes in Figure 8, we see that not only do both ORIGAMI and FOF size distributions shift toward smaller halos, but additionally, the ORIGAMI distribution becomes wider. We interpret this widening of the ORIGAMI size distribution as being

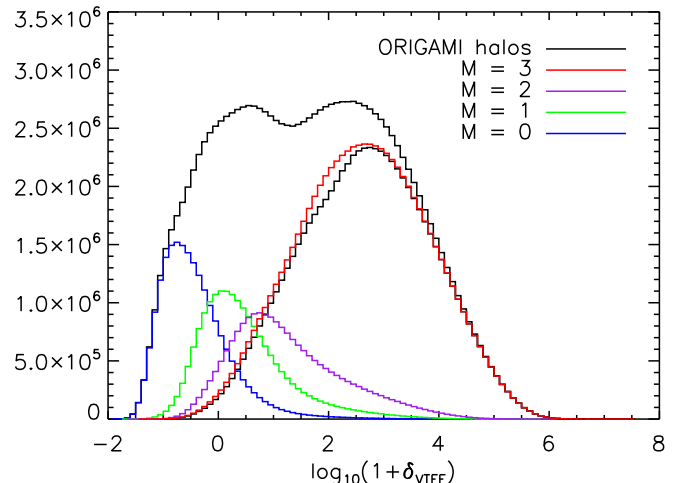


**Figure 13.** Distribution functions of the VTFE density for particles tagged as  $M = 0$  (void, *blue*),  $M = 1$  (wall, *green*),  $M = 2$  (filament, *purple*), and  $M = 3$  (halo, *red*), for the  $N = 512$  simulation.

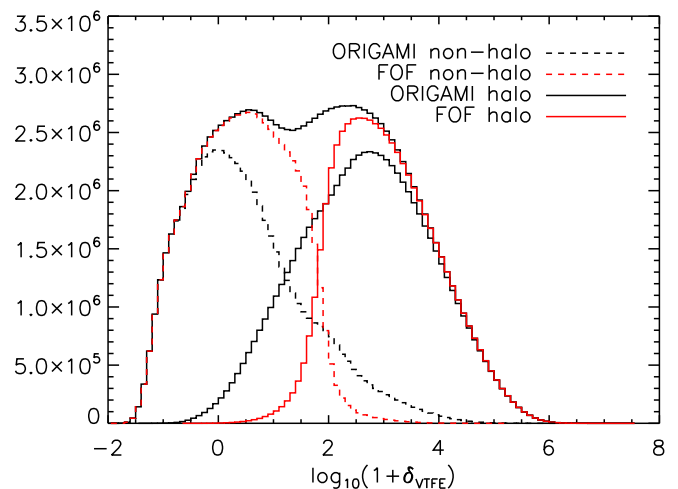


**Figure 14.** Distribution functions of the VTFE particle density for FOF and ORIGAMI halo and non-halo particles from the 512 simulation.

linked to the relative increase of low mass halos in the 512 simulation compared to FOF halos (Figure 6). The very small groups which had a mix of  $M = 2$  and  $M = 3$  particles in the 256 simulation, such that fewer than 20  $M = 3$  particles were grouped, have a greater percentage of  $M = 3$  particles in the 512 simulation, so more of these small groups are counted as full halos containing at least 20 particles.

As a final note regarding resolution, we mention that in ORIGAMI, the resolution with which structures are found need not correspond to the initial Lagrangian particle spacing, but could be a multiple of it. This could be useful in building a sort of hierarchical morphology tree from a single high-resolution simulation. Also, if there is much initial small-scale power in a high-resolution simulation, producing undesirably many small ORIGAMI halos, it could be useful to increase the Lagrangian resolution used for ORIGAMI morphology-tagging.

#### 4. DISCUSSION

The current version of the algorithm requires a Delaunay tessellation to group the halo particles into constituent halos, but we would like to stress that ORIGAMI is fundamentally a particle morphology tagger. The tagged halo (and filament, wall, and void) particles can be grouped in different ways; the tessellation method merely was expedient and sufficient for this paper. A Lagrangian-space method was also tried, which grouped halo particles that are connected on the initial Lagrangian grid as opposed to the final-conditions tessellation, but it was found that too many halo particles are connected on the Lagrangian grid which later form distinct structures. One possibility to improve the particle-grouping step would be to add bookkeeping that keeps track of *which* other particles a given particle has crossed paths with; though it is not necessarily true that these particles all end up in the same bound structure, the information could be useful.

Though a comparison of the ORIGAMI morphology classification to other methods is left to future work, we are encouraged by the results so far: by eye, it looks as if ORIGAMI does very well in identifying filament, wall, and void particles as well as halos. The task of grouping these particles into individual filaments, walls, and voids, however, will likely prove more challenging than for halos. It may be worthwhile to use ORIGAMI in concert with another morphology identification method that can be modified to take advantage of the ORIGAMI particle classification.

ORIGAMI is successfully able to calculate halo catalogs for cosmological dark matter  $N$ -body simulations, however, there may be some limits to its applicability. Due to its nature, ORIGAMI is unable to find groups in observations because it relies on information about the initial state of the system. Similarly, it would be difficult, though possible in principle, to apply ORIGAMI to simulations with baryons or with irregular (such as ‘glass’) initial conditions because the particles aren’t initially aligned on a regular grid. However, note that the idea of using caustics to identify the outer regions of groups has already been applied to measuring the masses of galaxy clusters (Diaferio 1999; Diaferio et al. 2005). Finally, ORIGAMI is currently unable to distinguish subhalo particles from their parent halo, though it is possible that using velocity information will allow ORIGAMI to identify substructure.

As mentioned in the introduction, the mathematical field of paper origami has developed quite recently (Lang 1996; Hull 1994, 2002, 2006). In so-called flat origami, the final product is constrained to lie in a plane after folding, likely with some regions in which many layers of paper overlap. A set of creases in the initial paper is only foldable into a flat origami design if the creases obey a set of laws.

Some of these laws are irrelevant to large-scale structure because of the different dimensionality and the inhomogeneous stretching that occurs, but a law that may be relevant is two-colorability. In two-dimensional flat origami, polygons in the paper must end up facing either up or down, so the tessellation formed by the initial crease pattern must be two-colorable, one color painting the “up” polygons, and the second color painting the “down.” In analogy, Lagrangian space can be tessel-

lated with three-dimensional regions bordered by caustics. In this case, we speculate that regions could be successfully colored according to their two possible orientations or chiralities, i.e. according to whether the three initially right-hand-oriented axes are left- or right-hand oriented. This issue will be the subject of a future study: two-colorability would be quite special for a three-dimensional tessellation, for which arbitrarily many colors (not only four, as in two dimensions) can in principle be required (e.g., Wilson 2002).

## 5. CONCLUSION

The ORIGAMI structure-finding algorithm identifies particles as belonging to a halo, filament, wall, or void by determining whether they have crossed paths with their Lagrangian neighbors along 3, 2, 1, or 0 orthogonal dimensions, respectively. In the present implementation, halo-classified particles that are connected on a Delaunay tessellation are grouped into individual halos, though in principle there are many ways in which halo particles may be grouped. Long strings or structures of over-connected halo particles are prevented by first requiring that halos contain at most one halo “core,” or set of connected halo particles, that are above some density threshold.

We have compared ORIGAMI halo catalogs to FOF catalogs at two different mass resolutions and found that the mass functions agree very well; more comparisons to other halo-finding algorithms are given in Knebe et al. (2011). Though the mass functions largely agree, ORIGAMI halos are in general much larger than FOF halos, suggesting that ORIGAMI halos are a bit more diffuse and spread out. Additionally, the smallest FOF halos contain many particles that ORIGAMI classifies as belonging to a filament, resulting in ORIGAMI finding fewer small halos. This result stresses the difference between a density-based definition of a halo and the ORIGAMI method of detecting the occurrence of shell-crossing.

The effect of increasing the simulation resolution is in general as expected, with more structures popping up at smaller scales. Both the ORIGAMI and FOF methods find a larger fraction of halo particles at a higher mass resolution, but this effect is greater for ORIGAMI. For the mass function, this results in ORIGAMI finding an increased fraction of low mass halos compared to FOF. Additionally, the ORIGAMI distribution of halo sizes gets wider as resolution increases, while the FOF distribution stays roughly the same shape, and both shift to smaller sizes. This resolution effect is not seen in the  $M_{200}$  mass function, suggesting that it largely occurs at the outer edges of the halos and for low-density halos, both of which have little effect on  $M_{200}$ .

With ORIGAMI, we have defined the boundary of a halo as being located at the outer phase-space caustic. This has produced some interesting differences in the sizes and general characteristics of ORIGAMI and FOF halos, which diagnostics that depend only on the central cores of halos tend to miss. In other algorithms, the definition of a halo edge usually depends strongly on a free parameter, but in ORIGAMI the definition of halo particles is parameter-free. Instead of depending solely on density, ORIGAMI finds halos by looking for folds in phase-space.

B.L.F. and M.C.N. thank Alex Knebe, Steffen Knollmann, Gustavo Yepes, and Justin Read for hosting the “Haloes going MAD” workshop at the beautiful La Cristalera de Universidad Autonoma de Madrid. We are grateful to Miguel Aragon-Calvo for providing the simulations and much help and feedback while this algorithm was being developed. The authors thank Peter Behroozi, Marcel Haas, David Larson, Guilhem Lavaux, Nuala McCullagh, and Istvan Szapudi for helpful discussions and comments. M.C.N. thanks Robert Lang for an inspiring colloquium about paper origami and further discussions. The authors acknowledge financial support from the Gordon and Betty Moore Foundation and the NSF OIA grant CDI-1124403.

## REFERENCES

- Abel, T., Hahn, O., & Kaehler, R. 2011, ArXiv e-prints, 1111.3944
- Anderhalden, D., & Diemand, J. 2011, MNRAS, 414, 3166, 1102.5736
- Aragón-Calvo, M. A., Jones, B. J. T., van de Weygaert, R., & van der Hulst, J. M. 2007, A&A, 474, 315, 0705.2072
- Aubert, D., Pichon, C., & Colombi, S. 2004, MNRAS, 352, 376, arXiv:astro-ph/0402405
- Behroozi, P. S., Wechsler, R. H., & Wu, H.-Y. 2011, ArXiv e-prints, 1110.4372
- Bertschinger, E. 1985, ApJS, 58, 39
- Bond, N. A., Strauss, M. A., & Cen, R. 2010, MNRAS, 409, 156, 1003.3237
- Davis, M., Efstathiou, G., Frenk, C. S., & White, S. D. M. 1985, ApJ, 292, 371
- Diaferio, A. 1999, MNRAS, 309, 610, arXiv:astro-ph/9906331
- Diaferio, A., Geller, M. J., & Rines, K. J. 2005, ApJ, 628, L97, arXiv:astro-ph/0506560
- Diemand, J., Kuhlen, M., & Madau, P. 2006, ApJ, 649, 1, arXiv:astro-ph/0603250
- Eisenstein, D. J., & Hut, P. 1998, ApJ, 498, 137, arXiv:astro-ph/9712200
- Elahi, P. J., Thacker, R. J., & Widrow, L. M. 2011, MNRAS, 418, 320, 1107.4289
- Fillmore, J. A., & Goldreich, P. 1984, ApJ, 281, 1
- Forero-Romero, J. E., Hoffman, Y., Gottlöber, S., Klypin, A., & Yepes, G. 2009, MNRAS, 396, 1815, 0809.4135
- Gardner, J. P., Connolly, A., & McBride, C. 2007, in Astronomical Society of the Pacific Conference Series, Vol. 376, Astronomical Data Analysis Software and Systems XVI, ed. R. A. Shaw, F. Hill, & D. J. Bell, 69
- Gottlöber, S., Klypin, A. A., & Kravtsov, A. V. 1999, in Astronomical Society of the Pacific Conference Series, Vol. 176, Observational Cosmology: The Development of Galaxy Systems, ed. G. Giuricin, M. Mezzetti, & P. Salucci, 418, arXiv:astro-ph/9810445
- Habib, S. et al. 2009, Journal of Physics Conference Series, 180, 012019
- Hahn, O., Porciani, C., Carollo, C. M., & Dekel, A. 2007, MNRAS, 375, 489, arXiv:astro-ph/0610280
- Hull, T. 2006, Project origami: activities for exploring mathematics, Ak Peters Series (A.K. Peters)
- Hull, T. C. 1994, Congressus Numerantium, 100, 215
- Hull, T. C. 2002, in The Proceedings of the Third International Meeting of Origami Science, Mathematics, and Education, ed. T. C. Hull (A.K. Peters), 29
- Klypin, A., & Holtzman, J. 1997, ArXiv Astrophysics e-prints, arXiv:astro-ph/9712217
- Knebe, A. et al. 2011, MNRAS, 415, 2293, 1104.0949
- Knollmann, S. R., & Knebe, A. 2009, ApJS, 182, 608, 0904.3662
- Kofman, L., Pogosian, D., & Shandarin, S. 1990, MNRAS, 242, 200
- Kofman, L., Pogosyan, D., Shandarin, S. F., & Melott, A. L. 1992, ApJ, 393, 437
- Lacey, C., & Cole, S. 1994, MNRAS, 271, 676, arXiv:astro-ph/9402069
- Landau, L. D., & Lifshitz, E. M. 1969, Mechanics, 2nd edn. (Oxford: Pergamon Press)
- Lang, R. J. 1996, in Proceedings of the twelfth annual symposium on Computational geometry, ed. S. Whitesides, SCG '96 (New York, NY, USA: ACM), 98–105
- Lukić, Z., Reed, D., Habib, S., & Heitmann, K. 2009, ApJ, 692, 217, 0803.3624
- Maciejewski, M., Colombi, S., Springel, V., Alard, C., & Bouchet, F. R. 2009, MNRAS, 396, 1329, 0812.0288
- More, S., Kravtsov, A. V., Dalal, N., & Gottlöber, S. 2011, ApJS, 195, 4, 1103.0005
- Neyrinck, M. C., Gnedin, N. Y., & Hamilton, A. J. S. 2005, MNRAS, 356, 1222, arXiv:astro-ph/0402346
- Peebles, P. J. E. 1980, The Large-Scale Structure of the Universe (Princeton, N.J.: Princeton University Press)
- Planelles, S., & Quilis, V. 2010, A&A, 519, A94, 1006.3205
- Press, W. H., & Schechter, P. 1974, ApJ, 187, 425
- Rasera, Y., Alimi, J.-M., Courtin, J., Roy, F., Corasaniti, P.-S., Füzfa, A., & Boucher, V. 2010, in AIP Conf. Ser., Vol. 1241, Invisible Universe, ed. J.-M. Alimi & A. Fuözfa, 1134–1139, 1002.4950
- Schaap, W. E., & van de Weygaert, R. 2000, A&A, 363, L29, arXiv:astro-ph/0011007
- Shandarin, S., Habib, S., & Heitmann, K. 2012, Phys. Rev. D, 85, 083005, 1111.2366
- Shandarin, S. F. 2011, J. Cosmology Astropart. Phys., 5, 15, 1011.1924
- Sheth, R. K., & Tormen, G. 1999, MNRAS, 308, 119, arXiv:astro-ph/9901122
- Springel, V., White, S. D. M., Tormen, G., & Kauffmann, G. 2001, MNRAS, 328, 726, arXiv:astro-ph/0012055
- Stadel, J. G. 2001, PhD thesis, UNIVERSITY OF WASHINGTON
- Sutter, P. M., & Ricker, P. M. 2010, ApJ, 723, 1308, 1006.2879
- Tweed, D., Devriendt, J., Blaizot, J., Colombi, S., & Slyz, A. 2009, A&A, 506, 647, 0902.0679
- Valageas, P. 2011, A&A, 526, A67, 1009.0106
- van de Weygaert, R., & Schaap, W. 2009, in Lecture Notes in Physics, Berlin Springer Verlag, Vol. 665, Data Analysis in Cosmology, ed. V. J. Martínez, E. Saar, E. Martínez-González, & M.-J. Pons-Bordería, 291–413
- Vogelsberger, M., & White, S. D. M. 2011, MNRAS, 413, 1419, 1002.3162
- Vogelsberger, M., White, S. D. M., Helmi, A., & Springel, V. 2008, MNRAS, 385, 236, 0711.1105
- White, S. D. M., & Vogelsberger, M. 2009, MNRAS, 392, 281, 0809.0497
- Widrow, L. M., & Kaiser, N. 1993, ApJ, 416, L71
- Wilson, R. 2002, Four colours suffice: how the map problem was solved, Allen Lane Science Series (Allen Lane)
- Zel'dovich, Y. B. 1970, A&A, 5, 84
- Zukin, P., & Bertschinger, E. 2010, Phys. Rev. D, 82, 104044, 1008.0639